Global investigation of the fine structure of the isoscalar giant quadrupole resonance

A. Shevchenko,[1,*] O. Burda,[1] J. Carter,[2] G. R. J. Cooper,[3] R. W. Fearick,[4] S. V. Förtsch,[5] H. Fujita,[2,6] Y. Fujita,[6]
Y. Kalmykov,[1,†] D. Lacroix,[7,8] J. J. Lawrie,[5] P. von Neumann-Cosel,[1,‡] R. Neveling,[5] V. Yu. Ponomarev,[1] A. Richter,[1]
E. Sideras-Haddad,[2] F. D. Smit,[5] and J. Wambach[1]

[1]*Institut für Kernphysik, Technische Universität Darmstadt, D-64289, Darmstadt, Germany*
[2]*School of Physics, University of the Witwatersrand, PO Wits, Johannesburg 2050, South Africa*
[3]*School of Earth Sciences, University of the Witwatersrand, PO Wits, Johannesburg 2050, South Africa*
[4]*Department of Physics, University of Cape Town, Rondebosch 7700, South Africa*
[5]*iThemba LABS, P. O. Box 722, Somerset West 7129, South Africa*
[6]*Department of Physics, Osaka University, Toyonaka, Osaka 560-0043, Japan*
[7]*GANIL, CEA and IN2P3, Boîte Postale 5027, F-14076 Caen Cedex, France*
[8]*Laboratoire de Physique Corpusculaire, ENSICAEN and Université de Caen, IN2P3-CNRS, Blvd du Maréchal Juin,
F-14050 Caen, France*

Fine structure in the region of the isoscalar giant quadrupole resonance (ISGQR) in ^{58}Ni, ^{89}Y, ^{90}Zr, ^{120}Sn, ^{166}Er, and ^{208}Pb has been observed in high-energy-resolution ($\Delta E_{1/2} \simeq$ 35–50 keV) inelastic proton scattering measurements at $E_0 = 200$ MeV at iThemba LABS. Calculations of the corresponding quadrupole excitation strength functions performed within models based on the random-phase approximation (RPA) reveal similar fine structure when the mixing of one-particle one-hole states with two-particle two-hole states is taken into account. A detailed comparison of the experimental data is made with results from the quasiparticle-phonon model (QPM) and the extended time-dependent Hartree-Fock (ETDHF) method. For ^{208}Pb, additional theoretical results from second RPA and the extended theory of finite Fermi systems (ETFFS) are discussed. A continuous wavelet analysis of the experimental and the calculated spectra is used to extract dominant scales characterizing the fine structure. Although the calculations agree with qualitative features of these scales, considerable differences are found between the model and experimental results and amongst different models. Within the framework of the QPM and ETDHF calculations it is possible to decompose the model spaces into subspaces approximately corresponding to different damping mechanisms. It is demonstrated that characteristic scales mainly arise from the collective coupling of the ISGQR to low-energy surface vibrations.

　　　　PACS number(s): 24.30.Cz, 21.60.Jz, 25.40.Ep, 27.80.+w

I. INTRODUCTION

Electric and magnetic nuclear giant resonances are well-known examples of the striking behavior of an interacting system of fermions to form collective modes [1]. Over the years, much experimental work has gone into establishing an understanding of the global behavior of their gross features, such as centroid energies and widths. It is generally accepted that the width Γ of the resonance mainly derives from two mechanisms: direct particle emission from one-particle one-hole (1p1h) configurations, leading to an escape width $\Gamma^\uparrow$, and the evolution of 1p1h configurations into more complicated two-particle two-hole (2p2h) and finally to $npnh$ states, giving rise to a spreading width $\Gamma^\downarrow$. This latter scheme implies a hierarchy of widths and time scales (an assumption underlying all transport theories [2–4]), resulting in a fragmentation of the giant resonance strength in a hierarchical manner [5]. An important theoretical problem is to explain the nature of couplings between the levels in this hierarchy and to predict the scales of the fragmentation of the strength that thus arise from it.

Indeed, over twenty years ago it became apparent from a high-energy-resolution inelastic electron scattering experiment [6] that there was considerable fine structure superimposed on the broad bump of the isoscalar giant quadrupole resonance (ISGQR) in ^{208}Pb. This phenomeon was later confirmed in inelastic proton scattering experiments [7]. Recent high-energy-resolution (p, p') measurements demonstrated the fine structure in a wide range of nuclei for the ISGQR [8]. It has also been observed in other types of resonances such as the isovector giant dipole resonance [9,10], the magnetic quadrupole resonance [11], and the spin-isospinflip Gamow-Teller (GT) mode [12], establishing fine structure as a generic phenomenon of nuclei.

Nevertheless, a serious experimental problem has been the quantitative extraction of the scales of this fragmentation. A lower limit on observable scales is set by the experimental resolution. Experimental studies of giant resonances are typically performed using particle beams with energies of several hundred MeV requiring magnetic spectrometers for the detection of scattered particles. By utilizing beam dispersion-matching techniques, energy resolutions of the order of a few tens of keV can be achieved. The problem then is to determine scales that occur between the limits set by the experimental

---

*Present address: AREVA NP GmbH, D-91052 Erlangen, Germany.
†Present address: Radium Lampenwerk, D-51688 Wipperfürth, Germnany.
‡vnc@ikp.tu-darmstadt.de

　　　　044305-1

resolution and the broad envelope of the resonances of the order of several MeV. A variety of methods have been proposed for their extraction [8,13–17], of which the wavelet analysis was shown to be most promising [18].

Here, we present a systematic study of the fine structure of the ISGQR in medium-mass to heavy nuclei. Characteristic scales are extracted from a wavelet analysis and compared to different microscopic approaches based on the random-phase approximation (RPA). A comprehensive analysis reveals that the observed scales indeed arise from the coupling of 1p1h to 2p2h states. However, in contrast to the schematic picture just discussed, multiple scales are observed in this single mixing step. As demonstrated in the following they can be induced by the collective coupling to low-energy phonons. This mechanism contributes significantly to the damping width of giant resonances in heavy nuclei [5,19]. Successes and limitations of the microscopic models in describing the observed characteristic scales of the fine structure are discussed.

The paper is organized as follows: In Sec. II we describe the measurement techniques used to obtain the experimental spectra. In Sec. III we apply the wavelet analysis to these data. The models and their application to our data are described in Sec. IV. Conclusions are given in Sec. V.

II. DATA

A. Experimental data

The experimental data were obtained by high-energy-resolution (p, p') measurements [8] using the K600 magnetic spectrometer of the cyclotron facility at iThemba LABS, Somerset West, South Africa. Data were taken at an incident proton energy of 200 MeV at scattering angles chosen to maximize the ISGQR cross section. A number of targets were used, as detailed in Table I. For ^{90}Zr and ^{208}Pb, extended angular distributions were measured to investigate the possible influence of the excitation of other multipoles in the region of the ISGQR by extracting of characteristic scales with the analysis described in the next section. Beam currents ranged from 5 to 25 nA depending on the target and kinematics.

The spectrometer was used in dispersion-matched mode. Initial settings were made using ion-beam transport programs taking into account the complete beam line together with the measured field map of the K600 spectrometer. The faint-

TABLE I. Summary of information on targets and scattering angles used.

Target	Laboratory Angles (degrees)	Density (mg/cm^2)	Enrichment (%)
^{208}Pb	6, 8, 10, 12.5	0.74, 6.0	>98
^{166}Er	8	1.8	>95
^{142}Nd	9	1.49	>95
^{120}Sn	8	4.5	>95
^{90}Zr	9.2, 11, 13	10.1	97.7
^{89}Y	9.2	1.9	>95
^{58}Ni	10	3.0	>95

beam technique [20] was used to find the optimum beam setting. A typical resolution of $\Delta E = 30$ keV (full width at half maximum, FWHM) was achieved. However, owing to cyclotron instabilities this could usually not be maintained for the duration of a typical measurement of the order of 12 hours. By monitoring the fields of the dipole magnets of the spectrometer using NMR probes, peak drifts were shown not to contribute to the variation of the energy resolution. The resolution was monitored using a thin (740 μg/cm^2) ^{208}Pb target. A 1° slit collimator was used at the entrance to the spectrometer, defining a solid angle $\Delta\Omega = 1.3$ msr. Overall energy resolutions varying between 35 and 50 keV (FWHM) were achieved during data taking with the use of a circular 4° entrance collimator to the spectrometer.

A 50-mm brass block was placed directly in front of the focal plane to suppress events from elastic scattering that otherwise would dominate the total count rates. These were limited to about 1 kHz by the dead time of the data acquisition system. The scattered particles then passed through two plastic scintillator paddles, which provided a trigger signal to the spectrometer and also allowed for particle identification. A set of vertical drift chambers (VDCs) served to measure the focal plane position. It consisted of two chambers in the dispersive direction with 198 wires each and a chamber in the nondispersive direction with 16 wires. The latter was used to monitor the vertical beam position.

B. Data analysis

The spectra used for the data analysis were reconstructed offline. The data were broken up into shorter sections. Each section was energy calibrated and then resummed to produce an excitation energy spectrum. This procedure minimized the energy drift from cyclotron instabilities and typically improved the energy resolution by several keV. Particle identification was performed using both time of flight (TOF) from the target position to the trigger paddles and energy loss measurements of the particles in the trigger paddles. As illustrated in Fig. 1, the correlation between the pulse height signals from both paddles allows an unambiguous distinction of protons from background (mainly photons).
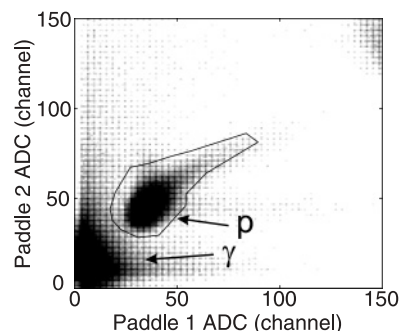

FIG. 1. Particle identification spectrum produced by the ΔE signals from scintillator paddles 1 and 2. Proton events can be clearly identified and separated from the background by a two-dimensional gate defined by the polygon.
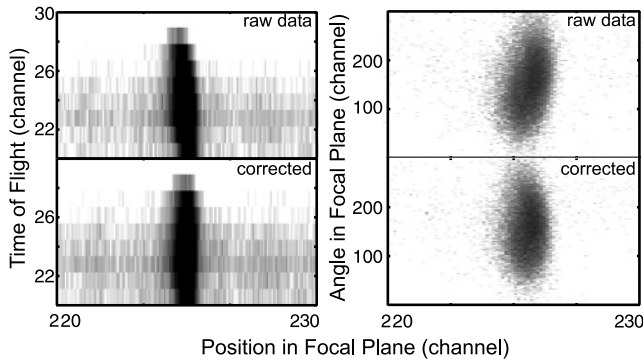
FIG. 2. Distribution of events from the ^{208}Pb(p, p') reaction in the focal plane corresponding to excitation energies around the first excited state in ^{208}Pb at $E_x = 2.615$ MeV as a function of either the time of flight (left) or the intersection angle (right) of the particle before (top) and after (bottom) application of position corrections.

The focal plane position of the scattered particle was reconstructed from drift times obtained from 3–9 adjacent wires of the vertical drift chamber. Some dependence of the focal plane position of spectral lines on the TOF on the intersection angle remains because of higher order abberations of the ion optics, as illustrated in the two top panels of Fig. 2. The example is taken from a ^{208}Pb(p, p') measurement and the part of the focal plane shown corresponds to the energy region around the first excited state in ^{208}Pb at $E_x = 2.615$ MeV. Corrections using polynomials of third order were applied, resulting in the straighter distributions shown in the bottom panels of Fig. 2. This led to another small gain in the overall energy resolution of the spectra.

Since the present study focuses on fine structure in the measured spectra, it is important to rule out significant contributions from artificial fluctuations resulting from variations of the efficiencies of the vertical drift chambers or specific features of the data analysis such as drift-time corrections. These can be excluded for the present data based on a number of arguments: Artificial structures should appear at the same position in all spectra measured with an identical setup. This is not observed. Furthermore, one can show the statistical nature of fluctuations in the continuum at high excitation energies, as demonstrated in the next section. Finally, as discussed in the following wavelet analysis is a sensitive method to locate regular structures and can be utilized to search for artificial fluctuations.

C. Spectra

As an example, we consider the ^{208}Pb(p, p') spectrum measured at $\Theta_p = 8°$ in the excitation energy region $E_x = 8$–12 MeV, where the ISGQR is located. It is presented in the bottom panel of Fig. 3 together with proton scattering data from IUCF [7] measured with the same kinematics (middle panel) and electron scattering data from the DALINAC [6] (top panel), both obtained with an energy resolution comparable to that of the present work. The proton scattering data show excellent agreement between the two spectra on a peak-by-peak basis. This is also true for the electron scattering spectrum, at least up to $E_x \simeq 10$ MeV. At higher E_x larger
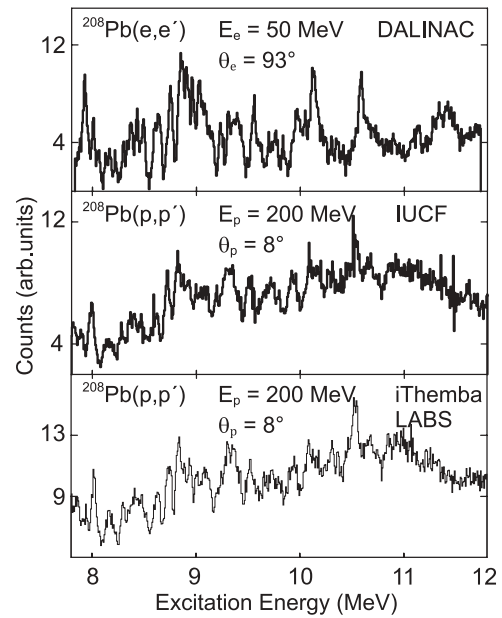

FIG. 3. Similarity of the structures observed in the three experiments on ^{208}Pb carried out in Darmstadt (top panel) [6], at IUCF (middle panel) [7], and recently at iThemba LABS (bottom panel).

differences between the fine structure in the (e, e') and (p, p') spectra are visible owing to the different selectivity of the two reactions. In the electron scattering data prominent excitation of $E1$ transitions from the low-energy tail of the IVGDR is expected whereas such transitions are only weakly excited in proton scattering. Nevertheless, the excellent agreement observed with two different probes already indicates that the fine structure is of genuine physical origin [7].

The difference between fluctuations from the fine structure in the giant resonance region and statistical fluctuations is demonstrated further in Fig. 4. The top panel illustrates the full range in excitation energy of the data up to $E_x \approx 20$ MeV. At $E_x < 8$ MeV, the spectrum is dominated by strong discrete transitions. The excitation energy range of the ISGQR (8–12 MeV) is expanded in the lower left plot. At
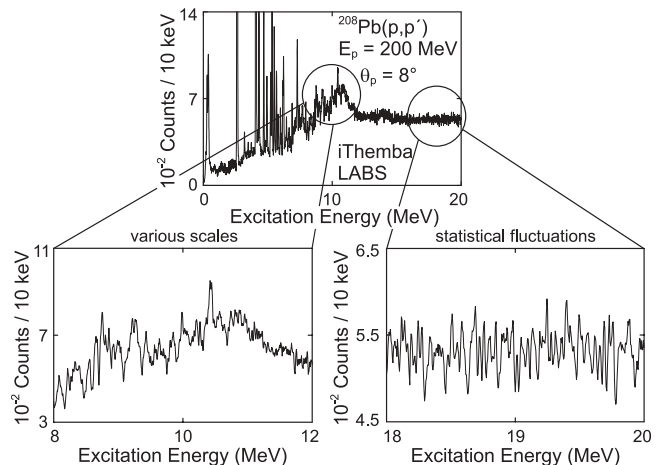

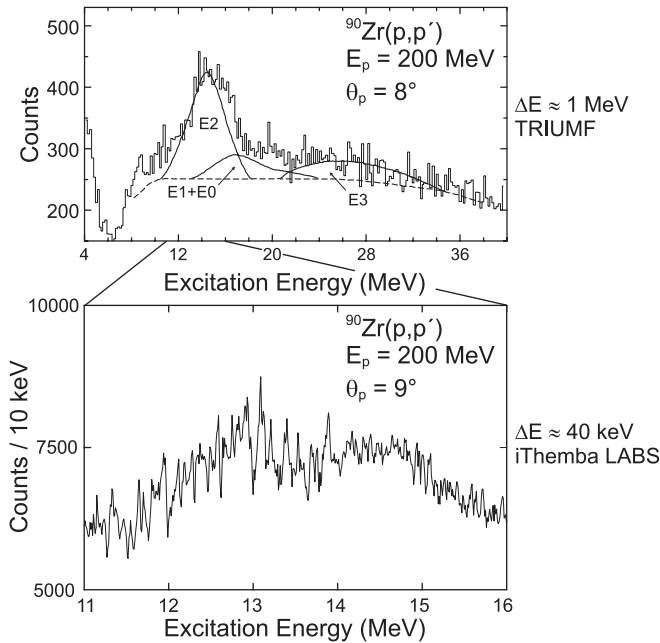FIG. 4. Different modes of fluctuations in the ^{208}Pb nucleus observed at different excitation energy ranges.

FIG. 5. Comparison of an earlier (p, p') experiment on the ISGQR in ^{90}Zr by Bertrand *et al.* [22] with the recently obtained high-energy-resolution data at iThemba LABS under similar kinematics. The broad bump in the upper spectrum around 14 MeV is interpreted as the ISGQR. The resolution of about 1 MeV is insufficient to observe any detailed structure. When measured with high energy resolution, the ISGQR region expanded in the lower part exhibits fine structure and a double-hump structure deviating from the typical assumption of a single Lorentzian.

FIG. 6. Experimental excitation energy spectra of the ISGQR in several nuclei—^{166}Er (top left), ^{120}Sn (top right), ^{89}Y (bottom left), and ^{58}Ni (bottom right)—measured at $E_p = 200$ MeV for scattering angles corresponding to a maximum of the $\Delta L = 2$ angular distribution. All cases show the appearance of fine structure, confirming this phenomenon as a global feature of the ISGQR.

even higher E_x the spectrum is rather structureless, and the excitation region 18–20 MeV is shown enlarged in the lower right plot in Fig. 4. There is a striking difference between the latter two, highlighting the fine structure in the ISGQR region as compared to the fluctuations in the high-excitation region. The statistical nature of the latter has been tested by calculating the autocorrelation function in a fluctuation analysis (see, e.g., Ref. [21] and references therein).

As an illustration of the impact of high-energy-resolution measurements we compare in Fig. 5 an early measurement of the ISGQR in ^{90}Zr using inelastic proton scattering by Bertrand *et al.* [22] with our measurement at iThemba LABS. In Ref. [22], the ISGQR was observed as a broad, smooth, roughly Lorentzian hump at about 14 MeV with a FWHM resolution of about 1 MeV. At high energy resolution (40 keV FWHM) considerable fine structure is revealed. In addition, the resonance is shown to have a double-humped structure, deviating from the typical assumption of a single Lorentzian made for the decomposition of hadron scattering spectra, as illustrated in the upper part of Fig. 5.

The experimental energy spectra of the other nuclei measured in this study are shown in Fig. 6 in an excitation energy range from 8 to 20 MeV covering the region of the ISGQR. In all nuclei, the enhancement of the cross sections in the ISGQR region is clearly visible and considerable fine structure is observed in all cases, confirming it as a global feature. This is especially remarkable for the case of the
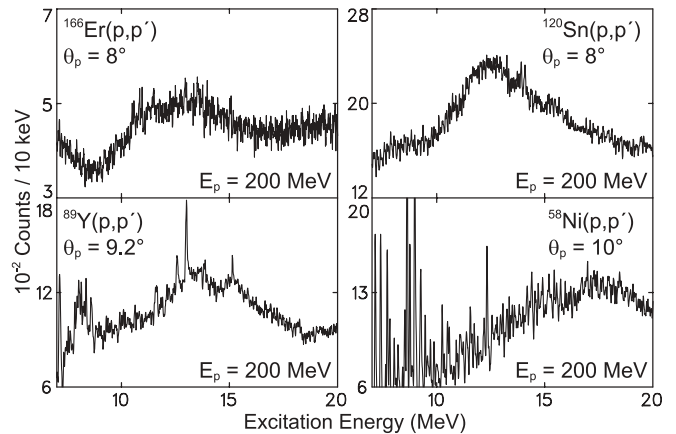
heavy, well-deformed nucleus ^{166}Er, where one might have expected these fluctuations to vanish because of the very high level density. Except for ^{120}Sn, all measured targets show a double-hump structure of the ISGQR. For ^{166}Er, this might be related to K splitting [23]. For spherical nuclei, a splitting of the ISGQR is well established in lighter nuclei such as ^{40}Ca [24,25] but the present results indicate that it persists toward heavier nuclei, at least up to mass $A = 90$. In the ^{89}Y data, very strong transitions are observed at $E_x \approx 13$ and 15 MeV on top of the resonance. These are most probably isobaric analog states, which are known to be pronounced in the $A \simeq 90$ mass region [26].

In the present experimental data it is generally observed that the magnitude of fine-structure fluctuations decreases with excitation energy. Another pronounced example of this phenomenon are the GT resonance data of Ref. [12]. Although we cannot offer at present a full explanation, it is—at least partially—due to the increasing level density. Another aspect may be that at some point one moves from the regime of fluctuations induced by the incoherent overlap of levels caused by the finite energy resolution to the regime of coherent Ericson fluctuations [27].

The dependence of the fine structure on scattering angle was investigated in more detail for the cases of ^{208}Pb and ^{90}Zr. As an example, the spectra of ^{90}Zr measured at scattering angles $\Theta_p = 9°, 11°$, and $13°$ are presented in Fig. 7. The fine structure visible in the different spectra is found to be largely identical, albeit with decreasing peak-to-background ratio for increasing scattering angles because one moves away from the optimum momentum transfer for $\Delta L = 2$ excitations. However, contributions from higher multipoles are weak.

III. WAVELET ANALYSIS

The experimental spectra described in Sec. II indicate that the fine structure of the ISGQR is a phenomenon observed
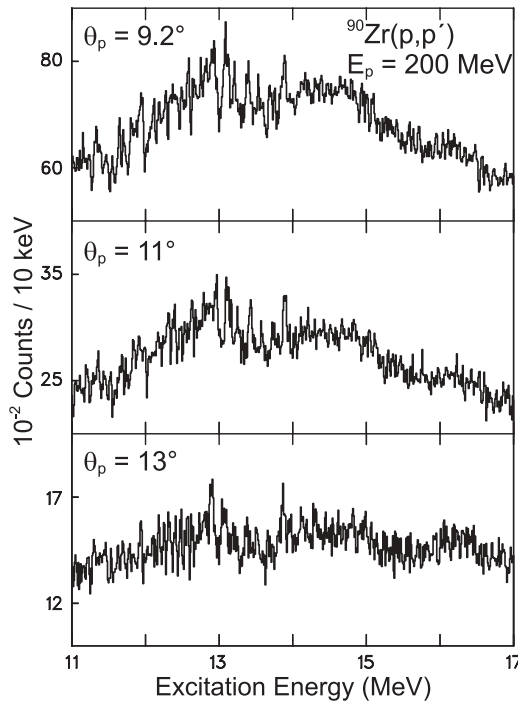
FIG. 7. Excitation energy spectra in the ^{90}Zr nucleus for different proton scattering angles at $E_p = 200$ MeV. A scattering angle of $\Theta_p = 9°$ corresponds to the maximum of the $\Delta L = 2$ angular distribution.

over a wide range of nuclei. To study the global nature of this structure we need to characterize the energy scales that are involved. The wavelet analysis provides a novel and extremely effective way to represent and analyze multiscale structures. Indeed, many physical systems are organized into "levels" or "scales" of some variable. A multiresolution or scalable mathematical representation may provide a simpler and more efficient extraction of the relevant degrees of freedom in physical systems [28]. Here a wavelet analysis based on the continuous wavelet transform (CWT) is performed to extract scales. A detailed discussion of the application of the CWT to nuclear giant resonances can be found in Ref. [18]; therefore we restrict ourselves to a brief presentation of the basic features of the technique.

A. Wavelet transform

A distinct feature of a wavelet analysis is the presence of a scaling parameter, which—loosely speaking—can be interpreted as the reciprocal Fourier frequency. The wavelet transform of some signal given here by a cross section $\sigma(E)$ is defined as its convolution with a (generally complex-conjugated) wavelet function $\Psi(E_x, \delta E)$,

$$C(\delta E, E_x) = \frac{1}{\sqrt{\delta E}} \int \sigma(E) \Psi^* \left(\frac{E_x - E}{\delta E} \right) dE. \quad (1)$$

The parameter δE scales (i.e., dilates or stretches) the function, whereas the parameter E_x shifts the wavelet position along the excitation energy so that the scale localization information becomes accessible. As a result of such a transformation,

one obtains a two-dimensional (2-D) distribution of wavelet coefficients $C(\delta E, E_x)$. These coefficients will be large at those scales δE and locations E_x where the form of the scaled and shifted wavelet $\Psi(x)$ has the biggest resemblance to the analyzed data sample $\sigma(E)$, and, if the scale of a wavelet function is very different from characteristic scales in the data at a given location, the coefficients will be small. Therefore, by studying this 2-D distribution of wavelet coefficients one can extract not only the values of the characteristic scales but also their locations, which are very important for nonstationary processes.

Another important advantage of the wavelet analysis is the freedom to use different wavelet functions and to find the appropriate one for a given problem, thereby extracting the required features most efficiently. To achieve a sparse representation of the signal using wavelet analysis, one has to select a function that best resembles the features of the signal to be studied. Thus, the shape of the wavelet function should be similar to that of the signal. However, the scale resolution of different wavelets must also be taken into account. Results from the use of the various different wavelets have been presented in Ref. [18]. It was found that the Morlet wavelet provides the best localization for the type of data presented in this paper.

The Morlet function is obtained by taking a periodic wave and localizing it with a Gaussian envelope,

$$\Psi_{\text{Morlet}}(x) = \pi^{-1/4} e^{ikx} \cdot e^{-x^2/2}. \quad (2)$$

The value of k specifies the number of "significant" sinusoidal oscillations within a Gaussian window. Formally, the function of Eq. (2) is not generally applicable as a wavelet. However, for $k \geqslant 5$ the condition of square integrability,

$$K_\Psi = \int_{-\infty}^{\infty} |\Psi^2(x)| dx < \infty, \quad (3)$$

is satisfied within the accuracy of computations with single-precision arithmetic. Higher values of k would slightly improve the scale resolution and in a limiting case one would end up with a Fourier spectrum. However, at the same time the scale localization property would be decreasing. For the analysis of nuclear giant resonance spectra described in the following, a value of $k = 5$ was found to provide the best compromise.

The scaling can be performed in continuous (CWT) or in discrete steps. The latter method allows for limited resolution only, but it provides a means to determine background contributions in the spectra in a model-independent way. This, in turn, enables the extraction of spin- and parity-resolved level densities in the energy region of the giant resonances [12,29].

B. Extraction of energy scales

All nuclei studied in the present work show the appearance of scales in the energy region of the ISGQR, as demonstrated in Figs. 8 and 9 for ^{90}Zr. Note that the square of the wavelet coefficients C [Eq. (1)] is plotted, and the blackness serves as a measure of their magnitude. The specific structure of
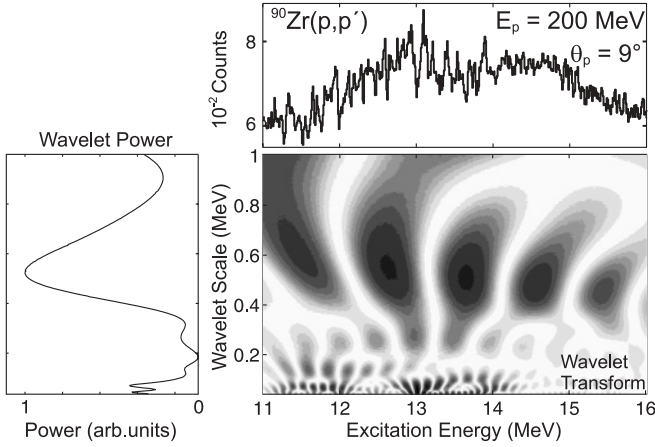
FIG. 8. The continuous wavelet transform of the ^{90}Zr(p, p') spectrum for $E_p = 200$ MeV and $\Theta_p = 9.2°$ using the Morlet wavelet [cf. Eq. (2)] for scale values up to 1 MeV.

alternating regions of large and small coefficients as a function of E_x results from the use of an oscillating function. To extract scales it is convenient to project onto the scale axis (the wavelet power spectrum). The maxima of the power spectrum are considered characteristic scales of the ISGQR in ^{90}Zr. Since the wavelet power increases with scale value, the scale axis in Fig. 8 is limited to 1 MeV for better visibility of characteristic scales at smaller energies.

As in the case of ^{208}Pb shown in Ref. [18], characteristic scales are also observed at energies larger than 1 MeV, as demonstrated in Fig. 9. In the present case two prominent scales with values of about 1.5 and 2.5 MeV are found, reflecting the double-hump structure of the ISGQR visible in Fig. 5 and the total width, respectively. At larger E_x (i.e., outside the resonance region) the wavelet coefficients are generally small.

As a second example we present the CWT of the data on ^{166}Er (see Fig. 10). Again, since the spectrum exhibits fine structure the CWT power spectrum is expected to show characteristic scales and this is indeed the case. We remark that the observation of fine structure in a heavy deformed nucleus comes somewhat as a surprise because of the very high level
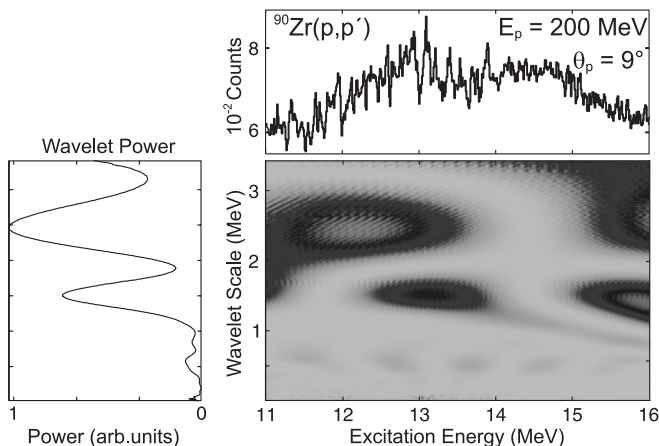

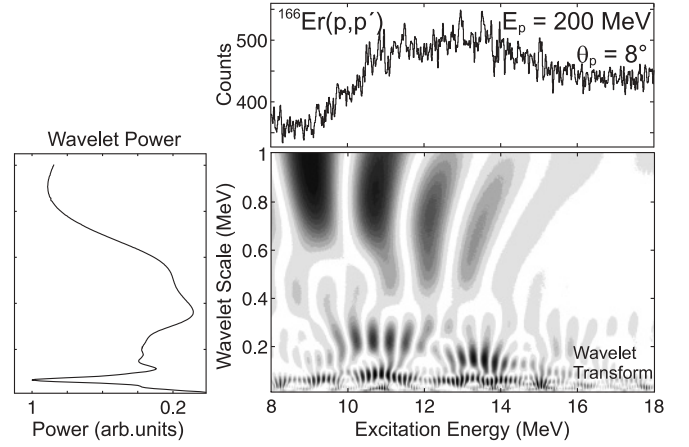FIG. 9. Same as Fig. 8 but for scale values up to 3.2 MeV.

densities of the order 10^7–10^{10} MeV^{-1} expected [30] in the region of the ISGQR. The corresponding large number of open channels in the continuum decay should damp the fluctuation signal. The smallest scale observed in the corresponding power spectrum is a trivial one: It arises from the experimental energy resolution. The same is true for all other spectra analyzed.

A summary of all deduced scales is given in Table II. As already pointed out in Ref. [8], these can be grouped empirically into three categories. In all nuclei one characteristic scale around 100 keV (I), several scales between 100 keV and 1 MeV (II) varying strongly between the investigated nuclei, and one or two scales at several MeV (III) are found. The latter result from the gross structure and the total width of the ISGQR, as already discussed for the example of ^{90}Zr. The two smaller scales obtained for ^{208}Pb agree favorably with those from an earlier analysis [17] based on the entropy index method (110 keV, 460 keV).

A question remains whether an artificial origin of some of the scales arising from specific properties of the VDC detectors can be excluded. Wavelet analysis is in fact a sensitive tool to test this. For example, the most likely regular structure expected to be observed in a VDC position spectrum is related to the wire spacing (4 mm in the present case). Under the present experimental conditions it corresponds to a spacing of about 160 keV when converted to an energy spectrum. In a CWT analysis, such a regular structure should show up as a prominent scale in all the spectra. No such scale

FIG. 10. The CWT of the ^{166}Er(p, p') spectrum for $E_p = 200$ MeV and $\Theta_p = 8°$ using the Morlet wavelet.

TABLE II. Summary of the characteristic scales deduced from the CWT analysis (in keV).

Nucleus	I	II	III
^{208}Pb	110	500	1500 2600
^{166}Er	150	250 880	2260 3260
^{142}Nd	130	420	1200 3200
^{120}Sn	80	220 330 470	1100 3200
^{90}Zr	70	140 260 540	2100 3100
^{89}Y	120	190 320 540 830	2100 3100
^{58}Ni	70	170 360 580 850	2800 4700

was observed. Furthermore, the continuum region at high excitation energies, where no physical scales are expected, indeed contributes negligibly only to the wavelet power spectrum, as demonstrated in Ref. [18] for the ^{208}Pb spectrum shown in Fig. 4.

Another question to address is whether the observed fine structure and characteristic scales really originate from the ISGQR or whether other resonances also contribute. It is well known that the strength distributions of the isoscalar giant monopole resonanace (ISGMR), the isovector giant dipole resonance (IVGDR), or the isoscalar giant dipole resonance (ISGDR) partially overlap with that of the ISGQR [1]. We have estimated their contributions to the spectra with distorted-wave Born approximation (DWBA) calculations, assuming a comparable exhaustion of the respective energy-weighted sum rules (EWSR). The results can be summarized as follows: Nuclear as well as Coulomb excitation of the IVGDR are negligble at the "large" angles studied here. The ISGMR has indeed the same angular distribution as the ISGQR except at very small angles, but for the same EWSR fractions the ISGMR (p, p') cross sections at angles of the first maximum of the ISGQR are always more than an order of magnitude smaller. The ISGDR is also expected to be weakly excited only at these kinematics.

The influence of other multipoles can also be tested by studying the evolution of power spectra for a given nucleus as a function of the scattering angle. This is illustrated for the case of ^{208}Pb, where data were taken for a larger angle range above and below the maximum of the $\Delta L = 2$ excitations, thereby enhancing contributions of other multipoles and suppressing the ISGQR. The results of the wavelet analysis for the ^{208}Pb target are shown in Fig. 11 for scattering angles 6°, 8°, 10°, and 12.5°, with the spectra on the left-hand side and wavelet power spectra on the right-hand side. The power spectrum is normalized so that the smallest scale (experimental resolution) has unit power. This normalization removes any dependency on the statistics of the spectra, and the spectra at different
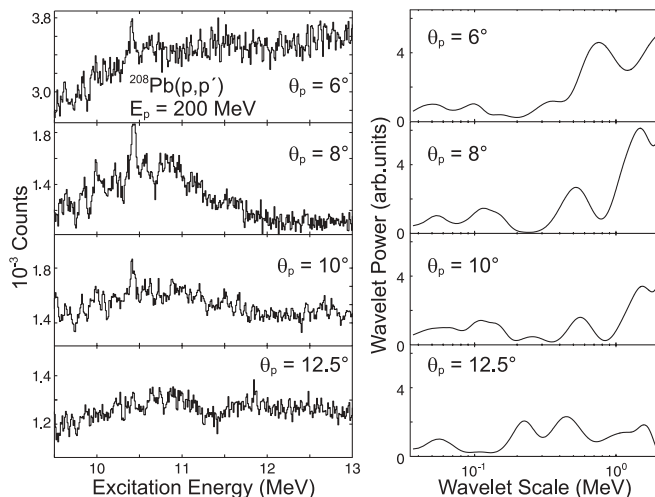
angles can be compared directly. The 6° spectrum contains considerable instrumental background, which appears at specific positions of the plane and is therefore not smoothly distributed over the energy spectrum. Thus, an interpretation of the scales observed in the corresponding power spectrum remains doubtful. The 310- and 700-keV scales extracted from this spectrum disappear at other scattering angles. A 110-keV scale increases in power as one moves to 8°. The scales present in the maximum of ISGQR cross section at 8° are getting weaker at larger angles, thereby supporting the hypothesis of their ISGQR origin. At 10° a new scale of 230 keV appears, and this becomes even stronger at 12.5°, whereas the 110-keV scale, in contrast, almost disappears. Thus, in the case of the ISGQR in ^{208}Pb, excitations with $\Delta L > 2$ may have some impact at larger scattering angles but do not affect the scaling information at the scattering angle corresponding to the maximum of $\Delta L = 2$ cross sections, on which the scales in Table II are based. This is also confirmed by a similar analysis of the ^{90}Zr data (Fig. 7).

A comparison of wavelet power distributions of the quadrupole resonance in the measured nuclei at angles close to the maximum of ISGQR excitation are shown in Fig. 12. Here, ^{166}Er is left out because of its intrinsic ground-state deformation, which leads to modifications of the ISGQR strength distribution owing to a strong low-energy component [23]. All the other nuclei studied are either doubly or semi-magic. The power distributions are all normalized to the largest individual value. Note that the wavelet power axis in Fig. 12 is logarithmic. Obviously, the relative weight of characteristic scales of categories I–III (as introduced earlier) varies significantly. However, the power at large scale values generally dominates. It is interesting to compare the odd and even $N = 50$ nuclei ^{89}Y and ^{90}Zr, respectively, where one might hope to learn something about effects from coupling to

FIG. 11. Power spectra of the ^{208}Pb(p, p') data from a CWT analysis at four different scattering angles. The maximum of the ISGQR cross section lies close to 8°. The ISGQR gets weaker at smaller and larger scattering angles.
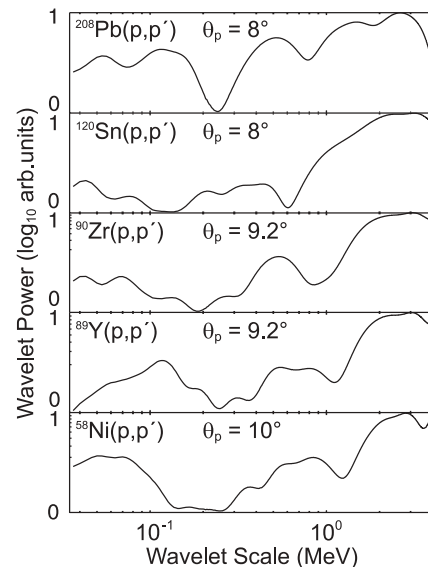

FIG. 12. Power spectra of data taken at scattering angles corresponding to the maximum of $\Delta L = 2$ excitations in the region of the quadrupole resonance for (top to bottom) ^{208}Pb, ^{120}Sn, ^{90}Zr, ^{89}Y, and ^{58}Ni.

an unpaired nucleon. For wavelet scales larger than 200 keV the power spectra are indeed quite similar, but differences are seen at smaller scale values around 100 keV. This might resemble the typical splitting of states resulting from the coupling of an unpaired particle or hole to states in the even-even core.

IV. MODEL CALCULATIONS

A. Origin of the fine structure

An interpretation of the physical nature of the characteristic energy scales obtained from experiment is possible only via a comparison with the results from microscopic calculations. Within the RPA model, where only 1p1h transitions are treated, the ISGQR strength is concentrated in just a few states. In the case of ^{208}Pb it is only one state, so that the response function shows no fine structure. Accordingly, as Fig. 13 demonstrates, the wavelet analysis does not detect any characteristic scales except a trivial scale from folding with a Gaussian of width of 50 keV (FWHM), put in to mimic the experimental resolution.

If one goes beyond the mean-field approximation and includes the coupling to 2p2h configurations the ISGQR strength in ^{208}Pb shown in the top frame of Fig. 14 fragments into many states and fine structure appears. By way of example, a second RPA (SRPA) calculation [17] described in detail in the following is shown here. The wavelet transform in the middle of Fig. 14 and the power spectrum on the left-hand side exhibit several characteristic scales. This fact is a demonstration of the significance of coupling to 2p2h configurations for the formation of fine structure and related characteristic scales, found in the experimental spectra. We remark that the maximum scale shown in Fig. 14 is restricted to 1 MeV, as for the experimental data in Figs. 8 and Fig. 10, to achieve better visibility of the CWT at small scales. A larger characteristic scale at 2.1 MeV representing the width of the resonance is also found.
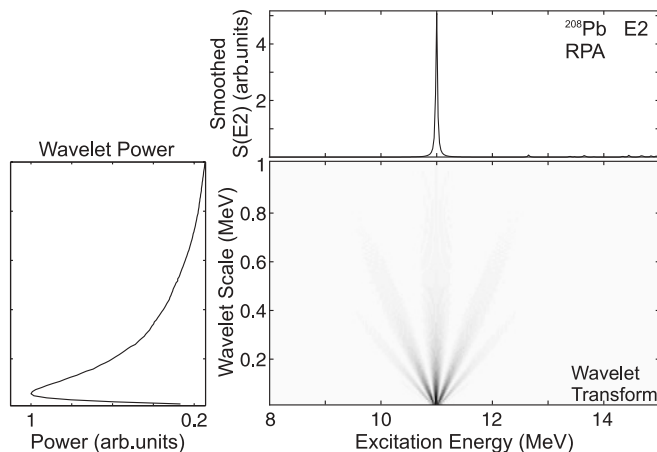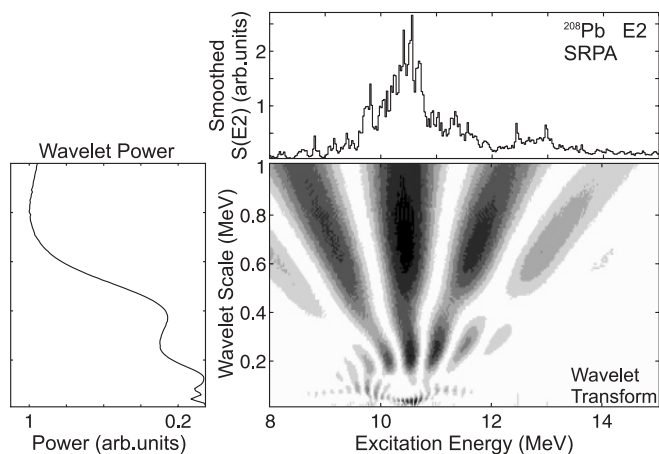

FIG. 14. The CWT analysis of the $E2$ response in ^{208}Pb predicted by an SRPA calculation [17].

B. Model dependence: the case of ^{208}Pb

Precise information on the scales present in the excitation energy spectra of giant resonances is of particular interest since it may help in understanding which mechanisms dominate the decay. However, the interpretation of the fine-structure scales is still far from being straightforward. A proper understanding of the observed subtle phenomena is impossible to accomplish without the help of modern sophisticated microscopic models.

For a physical interpretation of the results, one has to compare them with predictions for the strength functions of the collective mode studied. Examples are discussed in the next section where the doubly magic nucleus ^{208}Pb is investigated as a benchmark case. However, fine structure with its characteristic scales may serve as a stringent test for the validity and further improvement of the microscopic description of collective excitations in atomic nuclei. The experimental data set presented here on a number of different closed-shell nuclei provide a real challenge for modern microscopic nuclear structure calculations.

1. Mean-field approximation

The mean-field approximation can be described theoretically using a time-dependent Hartree-Fock (TDHF) approach [31,32]. It is based on the Vlasov equations of the time evolution of the one-body density matrix. This allows, in principle, any type of motion in the mean field, even those with large-amplitude oscillations. The full TDHF is actually extensively applied to collective vibrations and reactions but misses important two-body effects [33]. However, some of the effects can be incorporated in the small-amplitude version, which reduces the TDHF to the RPA limit.

In the RPA the nucleons move independently in an average potential. The "quasiparticles" interact via the mean field only. This excludes damping phenomena related to residual collisions of quasiparticles in the mean field. Nonetheless, there exists a damping mechanism, which is of purely quantum-mechanical origin. The damping effects contained in this description are usually referred to as *one-body dissipation*. One of them is Landau damping. In a finite nucleus it occurs

FIG. 13. The CWT analysis of the $E2$ response in ^{208}Pb predicted within the RPA. The strength is folded with a Gaussian of a width of 50 keV (FWHM) to mimic the experimental resolution. The strength is concentrated in one state, and there is no fine structure. The wavelet analysis also reveals no scales except the trivial one from the folding.

as a mixing between the collective state and the nuclear 1p1h excitations. In some cases, for example, in light nuclei, Landau damping may introduce a fragmentation of initial 1p1h doorway states and produce one or a few typical scales. A second damping mechanism is induced by direct particle emission from the initial 1p1h state, leading to an escape width $\Gamma^{\uparrow}$. However, qualitative agreement with high-energy-resolution experimental data can only be achieved by including two-body effects, such as in extended RPA approaches that go beyond the mean field. It has been shown that the coupling of 1p1h to 2p2h states gives rise to significant effects (see, e.g., Refs. [7,34,35]).

2. Models beyond the mean field

One-body dissipation from the nuclear mean field appears to be insufficient to describe the observed resonance broadenings. A so-called collisional damping or two-body dissipation is needed to account for the widths. An extension for these effects involves complicated parts of the two-body density matrix. There exist several approaches that have been proposed for the description of the damping of giant resonances, including internal mixing. Figure 15 summarizes microscopic calculations for the $E2$ response function in
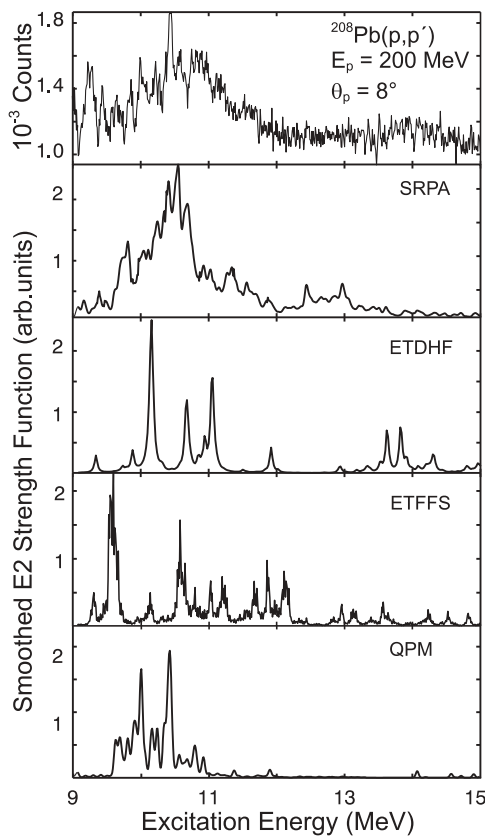

^{208}Pb in comparison with the recent data. Strength functions calculated within the SRPA [17], extended time-dependent Hartree-Fock (ETDHF) [36], extended theory of finite Fermi systems (ETFFS) [7,37], and the quasiparticle-phonon model (QPM) [38,39] are shown. The predictions differ substantially, each having a unique fragmentation of the collective strength over different ranges of excitation energies. A brief discussion of each approach follows.

3. Second RPA model

The small-amplitude limit of the generalized theory, the so-called second RPA, involves 1p1h as well as 2p2h excitations of the static ground state. The solutions of the SRPA equations are obtained numerically, using several approximation schemes, which separate out the most relevant degrees of freedom. The SRPA has been successfully used for the description of damping of giant resonances (see, e.g., Refs. [34,40]).

The SRPA calculation shown in Fig. 15 was taken from Ref. [17] and is based on the M3Y interaction [41] with an adjusted short-range part to reproduce the experimental centroids of the low-multipolarity electric giant resonances in ^{208}Pb. A truncation of the 2p2h configuration space was made at $E_x = 20$ MeV. At this limit one includes about 1.5×10^4 2p2h states. Details of the calculation are described in Ref. [42].

The truncation method used here focuses on diagonal matrix elements in the 2p2h subspace. Their distribution can be approximated by a Gaussian, by assuming random fluctuations. All configurations associated with matrix elements exceeding this Gaussian fit were included in the further analysis (about 3000 in the present example). The complex SRPA self-energy was chosen to attain a finite resolution similar to the experimental data. At the RPA level, the strength function consists essentially of a single collective state around 11 MeV as shown in Fig. 13. By introducing 2p2h components, the FWHM strongly increases and fine structure appears on top of the global shape. The gross shape of the experimental strength distribution is reproduced quite well (cf. Fig. 15).

4. Extended time-dependent Hartree-Fock model

A similar approach is realized within the ETDHF model, again by linearizing the extended TDHF equations so that one has only the low-amplitude vibrations. One accounts for the damping from the incoherent 2p2h decay in the form of a non-Markovian collision term [43,44] and the coherent coupling to 1p1h $\otimes$ phonon states, which originates from the response to a fluctuating one-body term. A review of the theoretical approach is given in Ref. [45]. The ISGQR strength distribution in ^{208}Pb shown in the third panel of Fig. 15 is obtained by employing an effective Skyrme interaction. A detailed discussion of the model calculations can be found for example in Refs. [35,36]. The experimental fragmentation is significantly underpredicted and part of the strength is shifted to a rather high excitation energy of about 14 MeV.

FIG. 15. The experimental spectrum of ^{208}Pb compared to microscopic model calculations for the ISGQR, including coupling to 2p2h states (top to bottom): SRPA [17], ETDHF [36], ETFFS [7], and QPM [39]. All models predict slightly different centroid energies, fragmentations, widths, and fine structure of the ISGQR.

5. *Extended theory of finite Fermi systems*

Another analogous method of describing damping of collective motion in atomic nuclei beyond the mean-field theory was developed in the framework of an extension of Migdal's theory of finite Fermi systems (ETFFS) where, in addition to the previously discussed damping mechanisms, namely Landau damping and more complex 1p1h ⊗ phonon or 2qp ⊗ phonon configurations (where qp stands for quasiparticles), the coupling to the single-particle continuum was included. This approach is based on a Green's function method. Here, one considers in a consistent way more complex 1p1h ⊗ phonon configurations beyond the RPA correlations. Moreover, these configurations are not only included in the excited states but also explicitly in the ground states of nuclei. A review of the theoretical approach is given in Ref. [37]. The result for the ISGQR in the ^{208}Pb nucleus [7] is shown in the fourth panel of Fig. 15. One can see that the coupling to the continuum leads to an additional broadening of the strength. This effect is believed, however, to be more significant for a proper description of resonance damping in light and medium-heavy nuclei, where the role of the continuum is known to be very important.

6. *Quasiparticle-phonon model*

Another approach permitting the inclusion of complex degrees of freedom equivalent to the SRPA is the QPM [46], which proved to be very successful in the microscopic description of collective excitations in ^{208}Pb [39,47,48]. In the QPM nuclear excitations are described by the creation of phonons made up from ph pairs. Because of pairing correlations, fractional occupation probabilities appear for a single-particle state j. These states are denoted as quasiparticle (qp) states. Since 1p1h pairs couple to an integer transfer of the quantum numbers, one can describe the transition as a creation of a boson, the so-called phonon. Note, however, that the term "phonon" is not reserved for collective states only but applies to transitions with rather pure 1p1h character as well. The model can account not only for one-phonon transitions but also for multiphonon excitations.

Applications of this model to collective transitions in ^{208}Pb are described, for example, in Refs. [38,39,47]. A two-step diagonalization procedure is applied. It allows the huge space of two-phonon configurations to be truncated by excluding the ones that have very small matrix elements. The omitted two-phonon configurations are believed to give almost no contribution to the damping process of collective one-phonon states. This leads to a significant reduction in the dimension of the matrices to be diagonalized. Another advantage of this calculation scheme is that it allows the disentanglement of various contributions to the damping of collective response in heavy nuclei by setting different truncation thresholds.

The resulting ISGQR strength distribution is shown in the bottom frame of Fig. 15. One can see that the centroid energy of the resonance and the fragmentation pattern observed experimentally are well reproduced. However, the width given by the QPM underestimates the experiment. Possible reasons
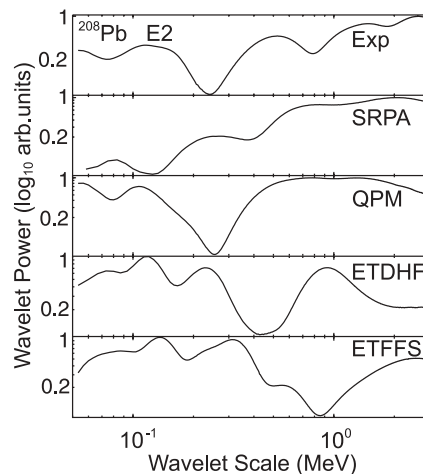

FIG. 16. Wavelet power spectra of the ISGQR in ^{208}Pb, from (top to bottom) experiment, SRPA, QPM, ETDHF, and ETFFS.

for this may lie in the interaction used, the neglect of coupling to the continuum, or in the truncation scheme.

7. *Comparison of extracted scales*

The high-energy-resolution data on the ISGQR in ^{208}Pb provide a remarkable opportunity for an in-depth comparison of theory and experiment because of the variety of microscopic calculations, including the coupling to 2p2h configurations with different truncation schemes and using different effective interactions, available for this doubly magic nucleus. This allows a detailed comparison to be made for the characteristic scales obtained from the experiment versus those from different model predictions, as is shown in Fig. 16. Wavelet analysis, therefore, represents a novel approach, providing a quantitative measure for the ability of different models to describe fine structure and characteristic scales.

Table III summarizes the values of characteristic scales deduced from the fine structure of ^{208}Pb in the region of ISGQR, as compared to those given by the microscopic model calculations just discussed. It should be noted that the values differ slightly from those given in an earlier analysis [8] because of an optimized treatment of boundary effects, as discussed in Ref. [18]. Again, results are classified according to the empirical categories I–III previously introduced. If one

TABLE III. Summary of the scales in ^{208}Pb observed experimentally compared to the different microscopic models that take into account coupling of 1p1h to 2p2h configurations.

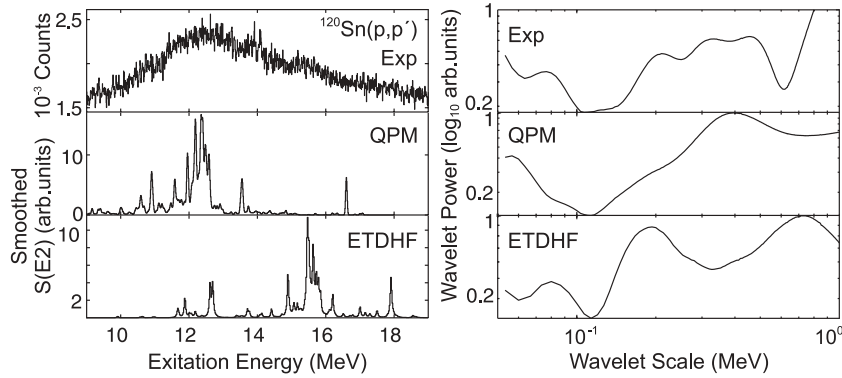| Category of scales	I	II	III
Experiment (keV)	110	500	1500 2600
Theories			
SRPA [17]	80	250 800	2100
ETDHF [36]	70 120	230 930	
ETFFS [37]	80 130	310 570	2500
QPM [39]	110	770	1400

FIG. 17. (Left) Experimental spectrum of the ^{120}Sn(p, p') reaction at the maximum of the ISGQR cross section vs QPM and ETDHF predictions for the ISGQR. (Right) Corresponding wavelet power spectra.

considers the largest scales (III) characterizing the width of the resonance, the closest values are given by the SRPA and ETFFS predictions. As for the other scales, of all the microscopic models the results of the QPM are the best in reproducing the experimental observation by reproducing the number of characteristic scales in categories I and II (one each) and reproducing the correct value of 110 keV for the smallest scale. All the other approaches find two scales in category II in contrast to the data.

The superior description of the fine structure by the QPM becomes even clearer when analyzing the power spectra in Fig. 16. In contrast to other models the pronounced minimum of the wavelet power between 200 and 300 keV in the experiment is correctly reproduced. Furthermore, the relative magnitude at small and large wavelet scales follows the experimental results quite well. The only shortcoming is observed at very large scales, since the experimental width is underpredicted. The wavelet power spectrum of the SRPA calculation provides a reasonable description at large scales (as one might have expected from good reproduction of gross features of the strength distribution) but fails for scales less than 800 keV. The EDTHF and ETFFS power spectra differ considerably from the QPM and SRPA results, and also from the data.

C. Other nuclei

Calculations have also been performed within the QPM and ETDHF for the ISGQR in ^{120}Sn, ^{90}Zr, and ^{58}Ni (QPM only) experimentally investigated in the present study. Results

for ^{120}Sn and ^{90}Zr are presented in Figs. 17 and 18, respectively, comparing the resulting strength distributions (left) and wavelet power spectra (right) to the data.

In both cases, QPM reproduces the experimental centroid energy whereas it is shifted to higher excitation energy by several MeV in the ETDHF results. However, both models fall short of describing the experimental widths. Correspondingly, the spectra contain little wavelet power at scales of several MeV, in contrast to the data (cf. Fig. 12). Therefore, the wavelet scale axes in Figs. 17 and 18 are restricted to 1 MeV. Overall, the QPM power spectra are closer to the data but deviations are more significant than in the case of ^{208}Pb. The QPM result for ^{58}Ni (not shown) is rather poor. This may be partly due to the neglect of direct decay becoming more important in lighter nuclei. However, it is also clear that the phonon approximation underlying the QPM approach is best justified in heavy nuclei.

D. Nature of scales: collective versus noncollective damping

Although the quantitative results of the models differ considerably, the success in reproducing at least the qualitative features of the experimental characteristic scales motivates attempts to extract their underlying physical nature from the model predictions. In the frameworks of the QPM and EDTHF calculations a decomposition of the full model space into subspaces, corresponding approximately to different damping mechanisms, was made. One such important mechanism contributing to the damping of the single-particle [49] as well as the collective response [19] in heavy nuclei is the coupling to low-lying surface vibrations, in the following called *collective*
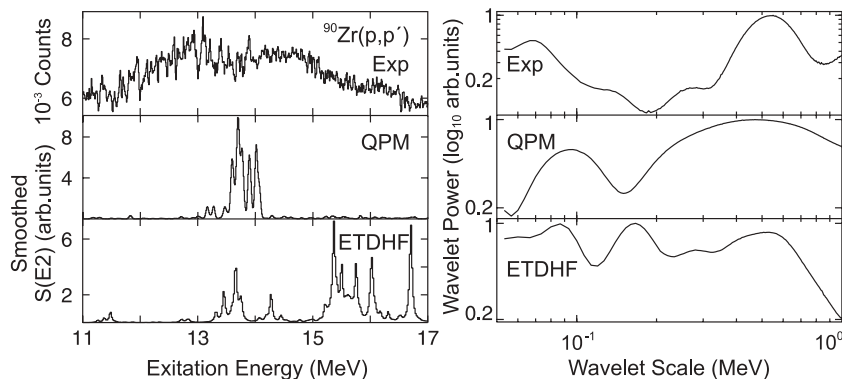

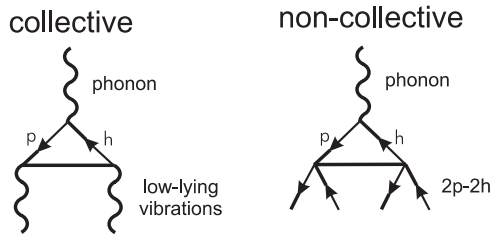FIG. 18. Same as Fig. 17 but for the ISGQR in ^{90}Zr.

FIG. 19. Collective vs noncollective damping mechanisms. The term "collective" corresponds to coupling to low-lying surface vibrations [19]. The noncollective contribution results from the mixing of initial 1p1h states with the large background of states with more complex wave functions.

damping. Another significant contribution may come from mixing of the initial 1p1h states with the large background of incoherent 2p2h states, hitherto called *noncollective* damping. These two mechanisms are depicted diagrammatically in Fig. 19.

As discussed in Ref. [8], the two contributions can be approximately disentangled as shown by considering the properties of the coupling matrix elements between the 1p1h and 2p2h configurations. This is discussed by way of example for the QPM results obtained on ^{120}Sn. The distribution of the coupling matrix elements V_{1p1h}^{2p2h} between 1p1h and 2p2h states is shown as a histogram in Fig. 20. The solid line shows a Gaussian distribution expected for fully chaotic systems from the Gaussian orthogonal ensemble (GOE) as predicted by random matrix theory (RMT) [50]. The value of the Gaussian width is adopted to match the data. One can see a large overshoot in the number of small matrix elements and in the wings of the distribution. The latter carry most of the collectivity of the excitations and are responsible for the collective damping. Similar features are observed in the analysis of off-diagonal interaction matrix elements in shell-model calculations [51]. An approximate separation of transitions contributing to collective and noncollective damping can be achieved by assigning subspaces and repeating the diagonalization within these subspaces. This is indicated in Fig. 20 as (i) and (ii) for noncollective and collective damping, respectively. A similar analysis has been performed with the ETDHF based on a perturbative treatment [45].

Calculations have been performed with the two models for ^{208}Pb, ^{120}Sn, and ^{90}Zr. Results for ^{208}Pb using the QPM
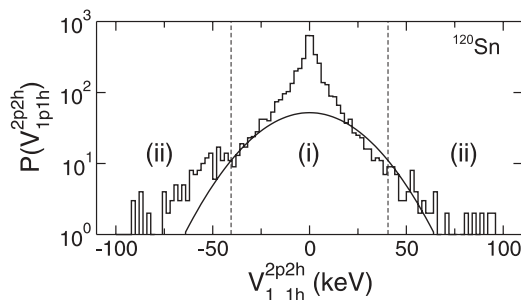

FIG. 20. Distribution of the coupling matrix elements V_{1p1h}^{2p2h} between 1p1h to 2p2h states in the QPM calculation for the $E2$ response in ^{120}Sn.

have already been presented in Ref. [8] but are included here (Fig. 21) for completeness and comparison to the corresponding result from ETDHF (Fig. 22). The resulting $E2$ strength functions are displayed in the left panel of Figs. 21 and 22. In both cases it is obvious that the fragmentation is dominated by the collective mechanism. However, one should be aware that the full calculation is not just the sum of the two contributions, and interference terms may play a role.

The corresponding wavelet power spectra are displayed in the right panels of Figs. 21 and 22, respectively. From the decomposition it is clear that in the case of ^{208}Pb all scales are already present in the collective part. The noncollective part shows wavelet power distributions broadly distributed over the range of scales. As pointed out in Ref. [8], the observed distribution can be well explained within a stochastic coupling approach in which level spacing distributions and coupling matrix elements are determined by RMT, thus supporting a generic nature of the noncollective damping.

Figures 23 and 24 present a similar disentanglement for the case of ^{120}Sn and provide essentially the same picture. All the scales observed in the full QPM prediction are already reproduced by including only collective damping with a broad distribution of wavelet power in the noncollective part, similar to what was obtained in ^{208}Pb. The same holds for the ETDHF results, although the noncollective part exhibits more structure in the power spectrum with a pronounced minimum around 200 keV and a local maximum around 100 keV. Nevertheless, the conclusion can be drawn that in heavy nuclei what is called *collective damping* is responsible for all the scales. In the noncollective part of ^{208}Pb and ^{120}Sn, a broad distribution of wavelet power is observed.

Conversely, the decomposition into a collective and a noncollective part in the medium-heavy nuclei ^{90}Zr and ^{58}Ni (see Figs. 25–27) shows an increased role of noncollective damping. The role of collective and noncollective mechanisms changes dramatically as one moves toward lighter nuclei.

However, the structure in the lighter nuclei is still not so well described by the models and their predictive power is therefore limited. The experimentally observed widths are grossly underestimated and the EDTHF result for ^{90}Zr shows a shift of the centroid by about 2 MeV. The noncollective damping mechanism is becoming more nongeneric as one goes to lighter systems. The results of the ETDHF model qualitatively confirm the findings from the QPM. However, the perturbative approach of the ETDHF leads to large shifts in the strength distributions, which might indicate strong interference effects of the two damping mechanisms, intrinsic within the model. This makes the results more difficult to interpret, as compared to the QPM calculations.

It is worth mentioning that the main peak position in ETDHF is largely influenced by the effective residual interaction used in the incoherent contribution, as illustrated in Appendix C of Ref. [45]. The discrepancy observed between the ETDHF results and experiment might eventually be reduced by modifying the parameters of the regularization technique of the zero-range interaction used in Refs. [35,36]. Therefore, a comparison with high-resolution experiments offers the possibility of getting information on the residual two-body interaction.
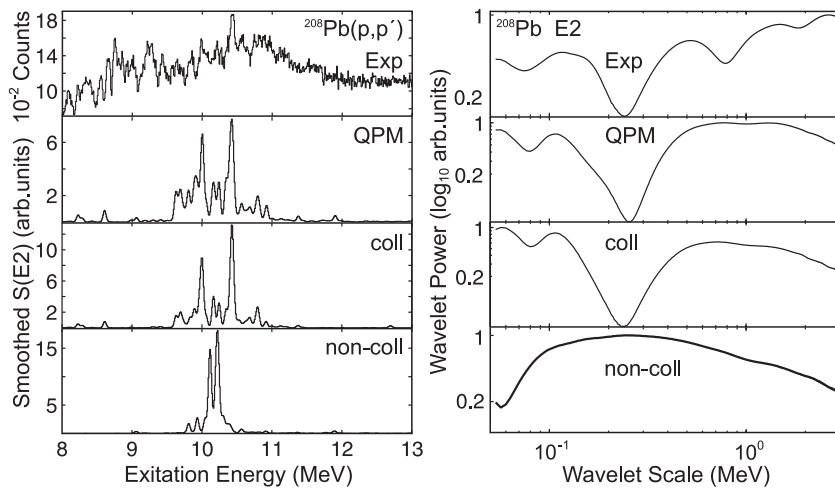
FIG. 21. (Left) Experimental spectrum of ^{208}Pb as compared to the QPM prediction for $E2$ strength and its decomposition into the collective and noncollective damping contributions. (Right) Corresponding wavelet power spectra.
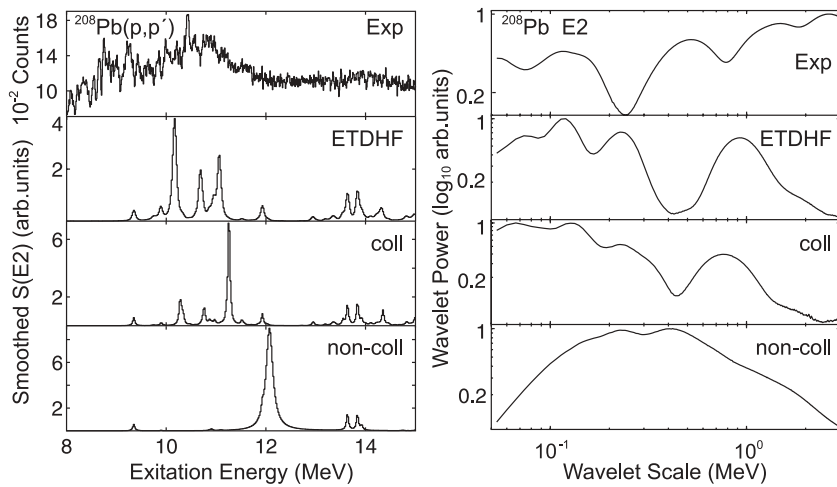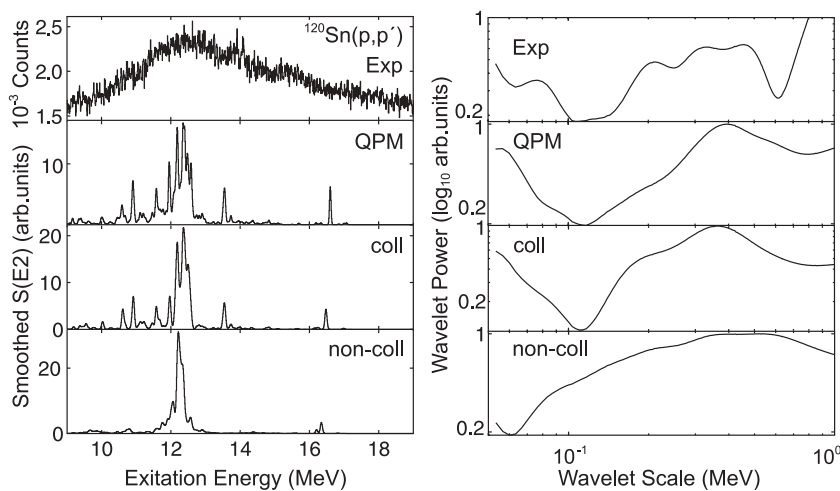

FIG. 22. Same as Fig. 21 but for the ETDHF calculation.
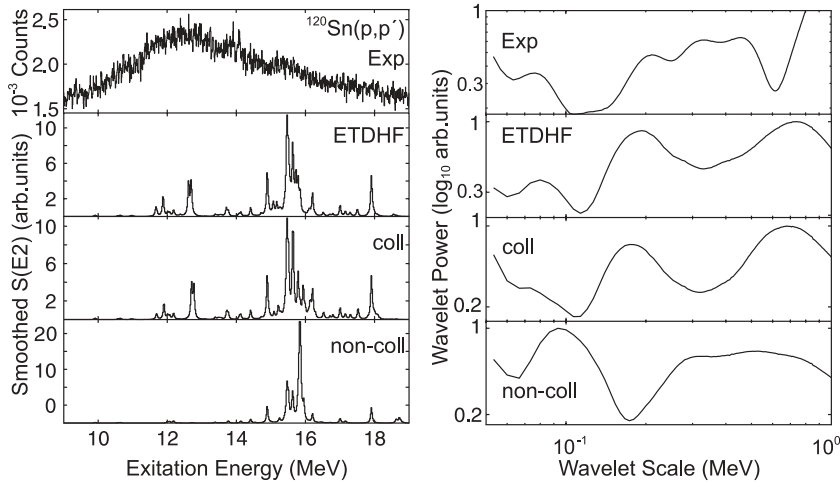

FIG. 23. Same as Fig. 21 but for ^{120}Sn.

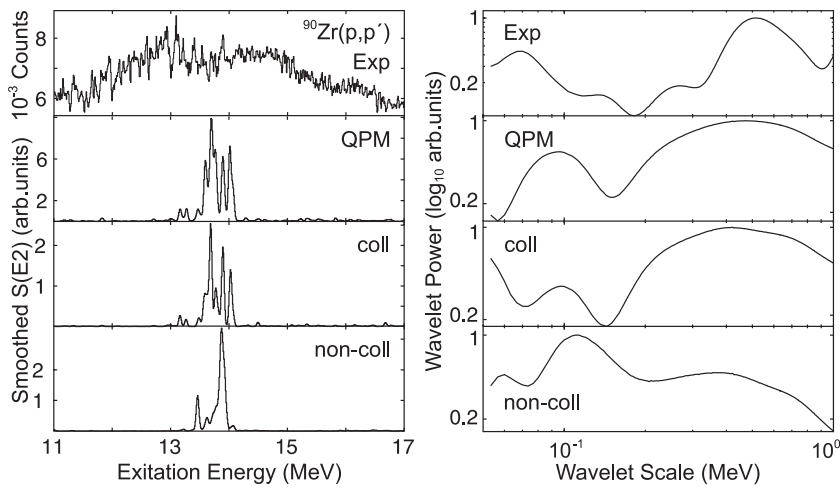FIG. 24. Same as Fig. 23 but for the ETDHF calculation.
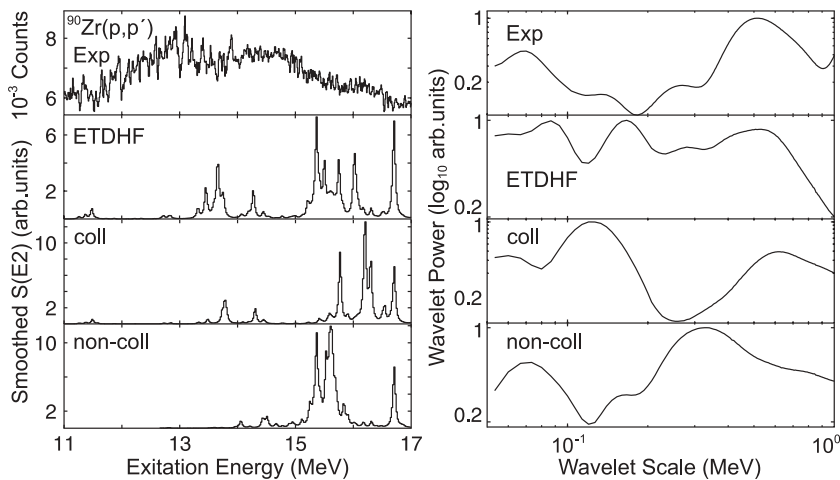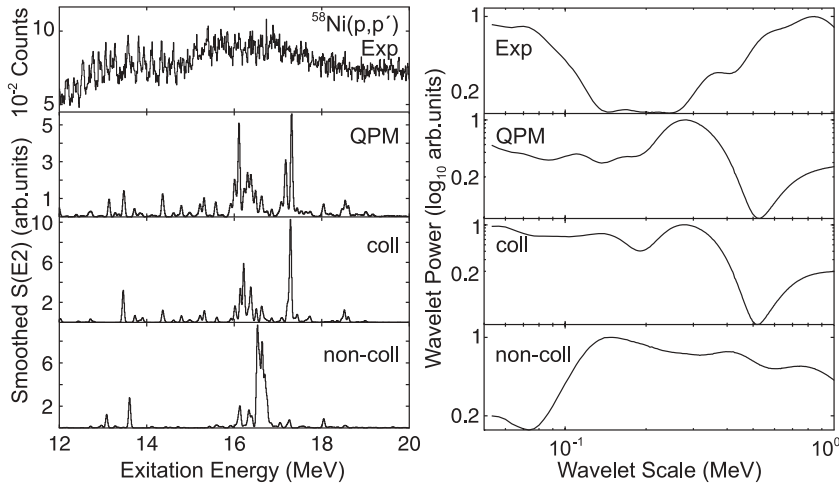

FIG. 25. Same as Fig. 21 but for ^{90}Zr.

FIG. 26. Same as Fig. 25 but for the ETDHF calculation.

FIG. 27. Same as Fig. 21 but for ^{58}Ni.

V. CONCLUSIONS

In the present work the phenomenon of fine structure in the region of the isoscalar giant quadrupole resonance is systematically investigated for the first time in a number of heavy and medium-heavy nuclei. High-energy-resolution inelastic proton scattering experiments were carried out at the iThemba LABS cyclotron facility in South Africa with an incident proton energy of 200 MeV. The data obtained with energy resolutions of $\Delta E \leqslant 50$ keV (FWHM) revealed the appearance of fine structure in all the nuclei studied (^{58}Ni, ^{89}Y, ^{90}Zr, ^{120}Sn, ^{142}Nd, ^{166}Er, and ^{208}Pb), thereby establishing the global character of this phenomenon.

The fine structure can be described by using characteristic energy scales, appearing as a result of the decay of collective modes toward the compound nucleus through a hierarchy of couplings to states of increasing complexity. A novel technique based on wavelet analysis is utilized for the extraction of the characteristic energy scales from the spectra. The global analysis of the available data shows the presence of three groups of scales, according to their values. To the first group belong the scales with values around and below 100 keV, which were detected in all the nuclei studied. The second group contains intermediate scales in the range of 100 keV to 1 MeV. These scales show large variations depending on the structure of the nucleus. The largest scales above 1 MeV, classified as belonging to the third group, describe the gross structure of the resonance (i.e., the width).

An interpretation of the observed scales is realized via the comparison with microscopic model calculations that include the coupling of the initial 1p1h excitations to more complex ones. A qualitative agreement of the experimentally observed scales with those obtained from the theoretical predictions supports the suggestion of the origin of fine structure to arise from the coupling to 2p2h states. Quantitatively, however, significant differences are observed for the values of scales given by different models for the case of ^{208}Pb. These differences are yet to be understood. They might be related to the employed effective interactions and/or the specific truncation schemes. The neglect of direct decay

seems to be of less importance since the best quantitative agreement is obtained with the QPM whereas the ETFFS result, which includes coupling to the continuum, is less satisfactory.

A more detailed study of the physical nature of the extracted scales is provided with the help of the quasiparticle-phonon model and extended time-dependent Hartree-Fock model, which allow the contributions from different damping mechanisms to be separated. The collective damping mechanism, which arises from the coupling to low-lying surface vibrations, is identified as the main source of the observed scales. This conforms with the doorway picture of the damping of giant resonances. Toward lighter nuclei, noncollective damping seems to be more relevant in describing the scales. However, the model predictions of the ISGQR become poorer and the impact of the approximations necessary for a separation of the two parts becomes more severe.

Clearly, many open questions remain, calling for future experimental and theoretical work. Experimentally, one would like to extend the systematics of the fine structure of the ISGQR to establish the role of deformation and to investigate the role of the escape width expected to become more relevant in lighter nuclei. Work along these lines is under way. In the near future one can also expect data of similar quality to the present work and over a broad range of nuclei for the IVGDR from high-energy-resolution inelastic proton scattering experiments at 0° [10]. Magnetic dipole and quadrupole resonances can be studied in transverse electron scattering [11,48,52]. Also, high-resolution studies of the GT$_-$ and GT$_+$ resonances are available [12,53,54].

On the theoretical side a better understanding of the origin of the large quantitative differences among different models is needed. This requires systematic studies on the role of interactions and truncation schemes of the model spaces. So far, only SRPA-type models have been used, which allow for large single-particle spaces but limit the complexity of wave functions to the level of 2p2h states. In medium-mass (fp shell) nuclei, $M1$ [52,55] and GT [56] resonances are well described by large-scale shell-model calculations. With respect to the question of model spaces this represents a

complementary approach: The single-particle spectrum is limited to one oscillator shell but many-particle many-hole configurations are included in the wave functions. Initial attempts to analyze the fine structure of $M1$ resonances with the CWT are encouraging [57]. Ultimately, as discussed in Sec. IV D, one may hope to utilize the information embedded in characteristic scales of the fine structure to pin down parts of effective interactions relevant to the description of collective modes.

[1] M. N. Harakeh and A. van der Woude, *Giant Resonances: Fundamental High-Frequency Modes of Nuclear Excitation* (Oxford University, Oxford, 2001).

[2] W. Cassing and U. Mosel, Prog. Part. Nucl. Phys. **25**, 235 (1990).

[3] P.-G. Reinhard and C. Toepffer, Int. J. Mod. Phys. E **3**, 435 (1994).

[4] Y. Abe, S. Ayik, P.-G. Reinhard, and E. Suraud, Phys. Rep. **275**, 49 (1996).

[5] P. F. Bortignon, A. Bracco, and R. A. Broglia, *Giant Resonances: Nuclear Structure at Finite Temperature* (Harwood Academic, Amsterdam, 1998).

[6] G. Kühner, D. Meuer, S. Müller, A. Richter, E. Spamer, O. Titze, and W. Knüpfer, Phys. Lett. **B104**, 189 (1981); G. Kilgus, G. Kühner, S. Müller, A. Richter, and W. Knüpfer, Z. Phys. A **326**, 41 (1987).

[7] S. Kamerdzhiev, J. Lisantti, P. von Neumann-Cosel, A. Richter, G. Tertychny, and J. Wambach, Phys. Rev. C **55**, 2101 (1997).

[8] A. Shevchenko, J. Carter, R. W. Fearick, S. V. Förtsch, H. Fujita, Y. Fujita, Y. Kalmykov, D. Lacroix, J. J. Lawrie, P. von Neumann-Cosel, R. Neveling, V. Yu. Ponomarev, A. Richter, E. Sideras-Haddad, F. D. Smit, and J. Wambach, Phys. Rev. Lett. **93**, 122501 (2004).

[9] S. Strauch, P. von Neumann-Cosel, C. Rangacharyulu, A. Richter, G. Schrieder, K. Schweda, and J. Wambach, Phys. Rev. Lett. **85**, 2913 (2000).

[10] A. Tamii, T. Adachi, J. Carter, M. Dozono, H. Fujita, Y. Fujita, K. Hatanaka, H. Hashimoto, T. Kaneda, M. Itoh, T. Kawabata, H. Matsubara, K. Nakanishi, P. von Neumann-Cosel, H. Okamura, A. Perez, I. Poltoratska, V. Yu. Ponomarev, L. Popescu, A. Richter, B. Rubio, H. Sakaguchi, Y. Sakemi, Y. Sasamoto, Y. Shimbara, Y. Shimizu, F. D. Smit, Y. Tameshige, M. Yosoi, J. Zenihiro, and K. Zimmer, Nucl. Phys. **A788**, 53c (2007).

[11] P. von Neumann-Cosel, F. Neumeyer, S. Nishizaki, V. Yu. Ponomarev, C. Rangacharyulu, B. Reitz, A. Richter, G. Schrieder, D. I. Sober, T. Waindzoch, and J. Wambach, Phys. Rev. Lett. **82**, 1105 (1999).

[12] Y. Kalmykov, T. Adachi, G. P. A. Berg, H. Fujita, K. Fujita, Y. Fujita, K. Hatanaka, J. Kamiya, K. Nakanishi, P. von Neumann-Cosel, V. Yu. Ponomarev, A. Richter, N. Sakamoto, Y. Sakemi, A. Shevchenko, Y. Shimbara, Y. Shimizu, F. D. Smit, T. Wakasa, J. Wambach, and M. Yosoi, Phys. Rev. Lett. **96**, 012502 (2006).

[13] J. Winchenbach, K. Pingel, G. Holzwarth, G. Kühner, and A. Richter, Nucl. Phys. **A410**, 237 (1983).

[14] H. Aiba and M. Matsuo, Phys. Rev. C **60**, 034307 (1999).

[15] H. Aiba, M. Matsuo, S. Nishizaki, and T. Suzuki, Phys. Rev. C **68**, 054316 (2003).

[16] D. Lacroix and P. Chomaz, Phys. Rev. C **60**, 064307 (1999).

[17] D. Lacroix, A. Mai, P. von Neumann-Cosel, A. Richter, and J. Wambach, Phys. Lett. **B479**, 15 (2000).

[18] A. Shevchenko, J. Carter, G. R. J. Cooper, R. W. Fearick, Y. Kalmykov, P. von Neumann-Cosel, V. Yu. Ponomarev, A. Richter, I. Usman, and J. Wambach, Phys. Rev. C **77**, 024302 (2008).

[19] G. F. Bertsch, P. F. Bortignon, and R. A. Broglia, Rev. Mod. Phys. **55**, 287 (1983).

[20] H. Fujita, G. P. A. Berg, Y. Fujita, K. Hatanaka, T. Noro, E. J. Stephenson, C. C. Foster, H. Sakaguchi, M. Itoh, T. Taki, K. Tamura, and H. Ueno, Nucl. Instrum. Methods Phys. Res. **A469**, 55 (2001).

[21] G. Hansen, B. Jonson, and A. Richter, Nucl. Phys. **A518**, 13 (1990).

[22] F. E. Bertrand, E. E. Gross, D. J. Horen, J. R. Wu, J. Tinsley, D. K. McDaniels, L. W. Swensen, and R. Liljestrand, Phys. Lett. **B103**, 326 (1981).

[23] M. Itoh, H. Sakaguchi, M. Uchida, T. Ishikawa, T. Kawabata, T. Murakami, H. Takeda, T. Taki, S. Terashima, N. Tsukahara, Y. Yasuda, M. Yosoi, U. Garg, M. Hedden, B. Kharraja, M. Koss, B. K. Nayak, S. Zhu, H. Fujimura, M. Fujiwara, K. Hara, H. P. Yoshida, H. Akimune, M. N. Harakeh, and M. Volkerts, Phys. Lett. **B549**, 58 (2002).

[24] F. Zwarts, A. G. Drentje, M. N. Harakeh, and A. Van Der Woude, Nucl. Phys. **A439**, 117 (1985).

[25] H. Diesener, U. Helm, G. Herbert, V. Huck, P. von Neumann-Cosel, C. Rangacharyulu, A. Richter, G. Schrieder, A. Stascheck, A. Stiller, J. Ryckebusch, and J. Carter, Phys. Rev. Lett. **72**, 1994 (1994).

[26] K. Shoda, M. Sugawara, T. Saito, and H. Miyase, Nucl. Phys. **A221**, 125 (1974).

[27] T. Ericson, Ann. Phys. (NY) **23**, 390 (1963).

[28] H. L. Resnikoff and R. O. Wells Jr., *Wavelet Analysis: The Scalable Structure of Information* (Springer-Verlag, New York, 2002).

[29] Y. Kalmykov, C. Özen, K. Langanke, G. Martínez-Pinedo, P. von Neumann-Cosel, and A. Richter, Phys. Rev. Lett. **99**, 202502 (2007).

[30] P. Demetriou and S. Goriely, Nucl. Phys. **A695**, 95 (2001).

[31] P. Ring and P. Schuck, *The Nuclear Many-Body Problem* (Springer-Verlag, New York, 1980).

[32] J. Speth (Ed.), *Electric and Magnetic Giant Resonances in Nuclei* (World Scientific, Singapore, 1991).

[33] C. Simenel, B. Avez, and D. Lacroix, lecture given at the "Joliot Curie" School, Maubuisson, 17–22 September 2007, arXiv:0806.2714v1.

[34] S. Drożdż, S. Nishizaki, J. Speth, and J. Wambach, Phys. Rep. **197**, 1 (1990).

[35] D. Lacroix, Ph. Chomaz, and S. Ayik, Phys. Rev. C **58**, 2154 (1998).

[36] D. Lacroix, S. Ayik, and Ph. Chomaz, Phys. Rev. C **63**, 064305 (2001).

[37] S. Kamerdzhiev, J. Speth, and G. Tertychny, Phys. Rep. **393**, 1 (2004).

[38] V. Yu. Ponomarev and P. von Neumann-Cosel, Phys. Rev. Lett. **82**, 501 (1999).

[39] N. Ryezayeva, T. Hartmann, Y. Kalmykov, H. Lenske, P. von Neumann-Cosel, V. Yu. Ponomarev, A. Richter, A. Shevchenko, S. Volz, and J. Wambach, Phys. Rev. Lett. **89**, 272502 (2002).

[40] C. Yannouleas, M. Dworzecka, and J. J. Griffin, Nucl. Phys. **A397**, 239 (1983).

[41] G. Bertsch, J. Borysowicz, H. McManus, and W. G. Love, Nucl. Phys. **A284**, 399 (1977).

[42] A. Mai, Diploma thesis, TU Darmstadt, 2000 (unpublished).

[43] K. Ando, A. Ikeda, and G. Holzwarth, Z. Phys. A **310**, 223 (1983).

[44] S. Ayik and M. Dworzecka, Phys. Rev. Lett. **54**, 534 (1985).

[45] D. Lacroix, S. Ayik, and Ph. Chomaz, Prog. Part. Nucl. Phys. **52**, 497 (2004).

[46] V. G. Soloviev, *Theory of Atomic Nuclei: Quasiparticles and Phonons* (Institute of Physics, Bristol, 1992).

[47] J. Enders, P. von Brentano, J. Eberth, A. Fitzler, C. Fransen, R.-D. Herzberg, H. Kaiser, L. Käubler, P. von Neumann-Cosel, N. Pietralla, V. Yu. Ponomarev, H. Prade, A. Richter, H. Schnare, R. Schwengner, S. Skoda, H. G. Thomas, H. Tiesler, D. Weisshaar, and I. Wiedenhöver, Phys. Lett. **B486**, 279 (2000).

[48] B. Reitz, A. M. van den Berg, D. Frekers, F. Hofmann, M. de Huu, Y. Kalmykov, H. Lenske, P. von Neumann-Cosel, V. Yu. Ponomarev, S. Rakers, A. Richter, G. Schrieder, K. Schweda, J. Wambach, and H. J. Wörtche, Phys. Lett. **B532**, 179 (2002).

[49] S. Galès, Ch. Stoyanov, and A. I. Vdovin, Phys. Rep. **166**, 125 (1988).

[50] T. Guhr, A. Müller-Groeling, and H. A. Weidenmüller, Phys. Rep. **299**, 189 (1998).

[51] V. G. Zelevinsky, Annu. Rev. Nucl. Part. Sci. **46**, 237 (1996).

[52] K. Langanke, G. Martínez-Pinedo, P. von Neumann-Cosel, and A. Richter, Phys. Rev. Lett. **93**, 202501 (2004).

[53] Y. Fujita, B. Rubio, T. Adachi, F. Molina, A. Algora, G. P. A. Berg, P. von Brentano, J. Buscher, T. Cocolios, D. De Frenne, C. Fransen, H. Fujita, K. Fujita, W. Gelletly, K. Hatanaka, M. Huyse, O. Ivanov, Y. Kudryavtsev, E. Jacobs, D. Jordan, K. Nakanishi, A. Negret, D. Pauwels, A. B. Perez-Cerdan, N. Pietralla, Z. Podolyak, L. Popescu, R. Raabe, Y. Sakemi, M. Sawicka, Y. Shimbara, Y. Shimizu, T. Shizuma, Y. Tameshige, A. Tamii, P. Van den Bergh, J. Van de Walle, P. Van Duppen, M. Yosoi, and K. O. Zell, J. Phys. G **35**, 014041 (2008).

[54] D. Frekers, Prog. Part. Nucl. Phys. **57**, 217 (2006).

[55] R. W. Fearick, G. Hartung, K. Langanke, G. Martínez-Pinedo, P. von Neumann-Cosel, and A. Richter, Nucl. Phys. **A727**, 41 (2003).

[56] E. Caurier, K. Langanke, G. Martínez-Pinedo, and F. Nowacki, Nucl. Phys. **A653**, 439 (1999).

[57] I. Petermann, K. Langanke, G. Martínez-Pinedo, P. von Neumann-Cosel, F. Nowacki, A. Richter, and A. Shevchenko (to be published).